1.5 Search for X-ray-Induced Acceleration of the Decay of the 31-Yr Isomer of ^{178}Hf

Releasing the energy stored in an isomeric nuclear state in a controlled way with an atomic or electromagnetic trigger is an attractive speculation: the energy gain is on the order of the ratio of nuclear/atomic energies (i.e., MeV/keV). (Nuclear isomers are loosely defined as excited nuclear states with lifetimes longer than 10^{-9} s.) Nuclear isomers, therefore, represent an opportunity for a stand-alone energy source if suitable schemes for trigger and control of the energy release can be found. Potential applications include space drive, as well as very bright gamma-ray sources. The nucleus ^{178}Hf has a nuclear isomer with excitation energy of 2.447 Me. The 2.447 MeV isomeric state decays slowly (31 year half life) to the nearby state at 2.433 MeV. This J = 13^- state then loses energy in a rapid ($\sim 10^{-12}$ s) gamma-ray cascade ending at the 8^- rotational band head, which in turn decays via the ground-state rotational band cascade. The gamma-ray cascade is delayed at the 8^- state at 1.147 MeV, since the 8^- state is also isomeric, with a half-life of 4 s.

Reports of triggered decay of the ^{178}Hf isomer induced by x-rays delivered by a dental x-ray machine have been made (Collins et al., 1999). Enhancements amounting to 1-2% in the isomer decay rate had been reported for various gamma rays in the cascade. The reported integrated cross section for triggering the decay is 10^{-21} cm^2 keV, so large as to demand new physics. A collaboration involving LANL, LLNL, and ANL have sought to verify these reports taking advantage of the intense photon flux available at the APS beamline 1-ID, using white beam from a tapered undulator source. No induced decay was observed. The upper limits for the energy-integrated cross section for such a process, over the range of x-ray energies 20-60 keV, are less than 2×10^{27} cm^2 keV, below the previously reported values by more than 5 orders of magnitude.

1.6 X-ray Microscopy and Microtomography

Since the last *Experimental Facilities Division/User Program Division Technical Progress Report* (ANL/APS/TB-38, 2000), the Micro-Techniques Group (now called the X-ray Microscopy Group) has continued to focus its efforts in the x-ray microscopy field. Application emphases were mainly in the biological/biomedical, environ-mental, and materials areas.

Novel x-ray microscopy experiments in the biomedical and environmental sciences continued to thrive. This was facilitated by operating two hard x-ray microprobes in parallel, with microfluorescence taking up ~40% operation of the 2-ID-D microprobe, and ~80% of the 2-ID-E side-branch microprobe. The high elemental sensitivity and spatial resolution of these instruments enabled trace elemental analyses in tissues, eukaryotic cells, and microorganisms at naturally occurring concentrations or at clinically relevant doses. Applications included studies of Pt- and Cu-derivative drug metabolism and Cr-induced carcinogenesis, metal contaminants in microbes at mineral surfaces and in marine and freshwater environments, metal distribution during cellular processes, and transfection of nanocomposites in cells. To explore these and future applications, we held a workshop on 14-15 May 2001, titled "Biological Applications of X-Ray Microbeams" (Lai et al., 2002). About 50 current and potential users attended. Other imaging modalities also flourished,

including microtomography optimized for high throughput, submicron-resolution phase tomography.

1.6.1 Transfection of TiO_2–Oligonucleotide Nanocomposites into Mammalian Cells

Nanotechnology can provide new capabilities for intracellular manipulation. For instance, hybrid complexes of TiO_2 nanoparticles and biopolymers can be used to remodel target DNA through the use of the photoelectrical properties of TiO_2 and the electrochemical properties and biological selectivity of the attached biopolymers. In particular, a polymerase chain reaction (PCR) with one oligonucleotide primer bound to TiO_2 nanoparticles shows (1) DNA bound to nanocomposite retains sequence-specific hybridization capability, (2) DNA-TiO_2 nanocomposites can participate in enzymatic reactions, and (3) illumination of nanocomposites causes breakage in the attached DNA within a short distance (few bp) from the nanoparticle. Thus the nanocomposites can be introduced into living cells, targeted to specific subcellular sites, and subsequently used as platforms for initiation of intracellular processes.

A group led by G. Woloschak (ANL/BIO) and M. Thurnauer (ANL/CHM) introduced TiO_2 (4.3-nm-diameter) nanoparticles alone or in combination with "free" oligonucleotides into mammalian cells *in vitro*, using standard transfection methods. We mapped the location and quantity of Ti in the cells using scanning x-ray fluorescence microscopy at the 2-ID-D beamline (Figs. 1.14 and 1.15). Chi-square analysis of the data showed an association of transfection success and addition of free oligonucleotides to Ti nanocomposites during transfection. Further-more, free oligonucleotides that were identical to the ones bound to TiO_2 nanoparticles produced fewer cells displaying the Ti signal then those cells transfected with Ti nanocomposites and heterologous free oligonucleotides. This showed that nanocomposites can be introduced into cells using standard transfection methods and can then translocate into the cell nuclei. X-ray microfluorescence is crucial in quantifying the success rate of transfection and revealing the intracellular distribution of the nanocomposites.

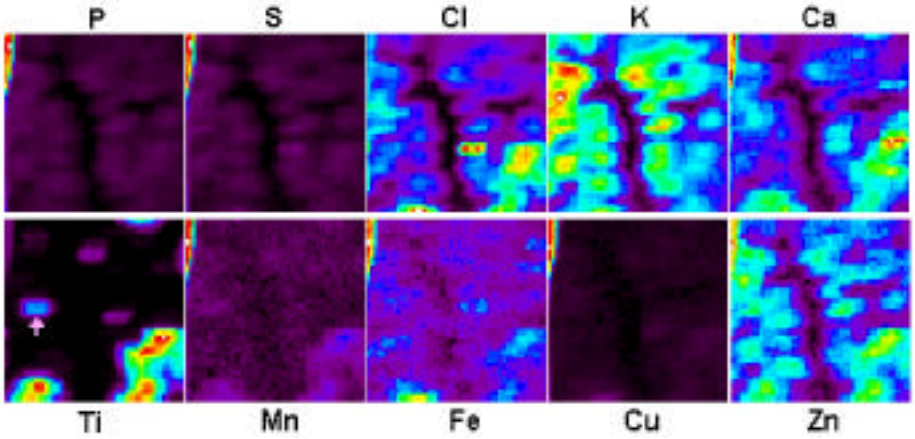

Fig. 1.14. X-ray fluorescence maps of several elements in a 90 µm × 90 µm area containing 28 HL60 cells transfected with TiO_2-oligonucleotide nanocomposites. The Ti map shows that seven cells contain Ti as a consequence of transfection.

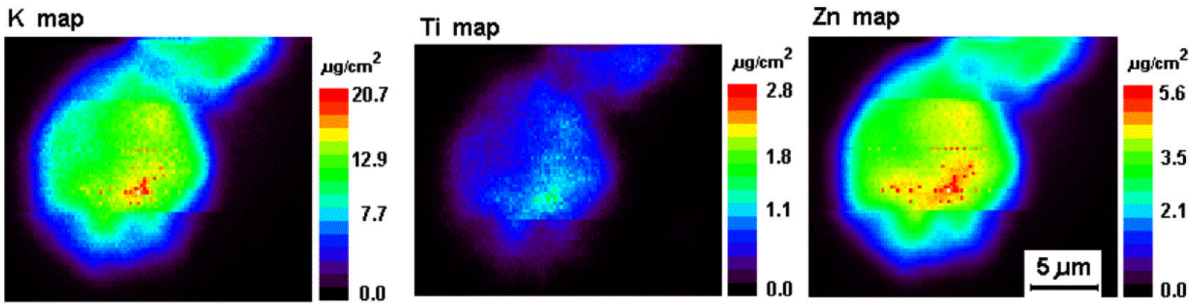

Fig. 1.15. High-resolution elemental maps of a 12 μm × 12 μm area of a single nucleus containing 3.6×10^6 nanoparticles. This nucleus was isolated from a whole cell transfected with R18Ss-TiO_2 nanocomposite and a free R18Ss oligonucleotide.

1.6.2 Trace Metal Contents of Individual Marine Protists

Over the past two years, B. Twining, S. Baines (SUNY-Stony Brook), and ourselves have used the 2-ID-E microprobe to map and quantify the trace elemental composition of single-celled microorganisms in the planktonic community. Accumulation of trace elements, such as Si, Fe, Cu, and Zn, by planktonic protists can influence the growth of primary producers (algae and phyto-plankton), elemental oceanic residence times, and metal bioaccumulation in aquatic food chains. Iron is of particular interest as it limits phytoplankton production in large oceanic regions. When Fe limits the growth of diatom cells, the cellular Si contents and thus sinking rates also change. Accumulation of Fe by protists thus influences the contribution of Fe-limited regions to oceanic C sequestration and global climate dynamics.

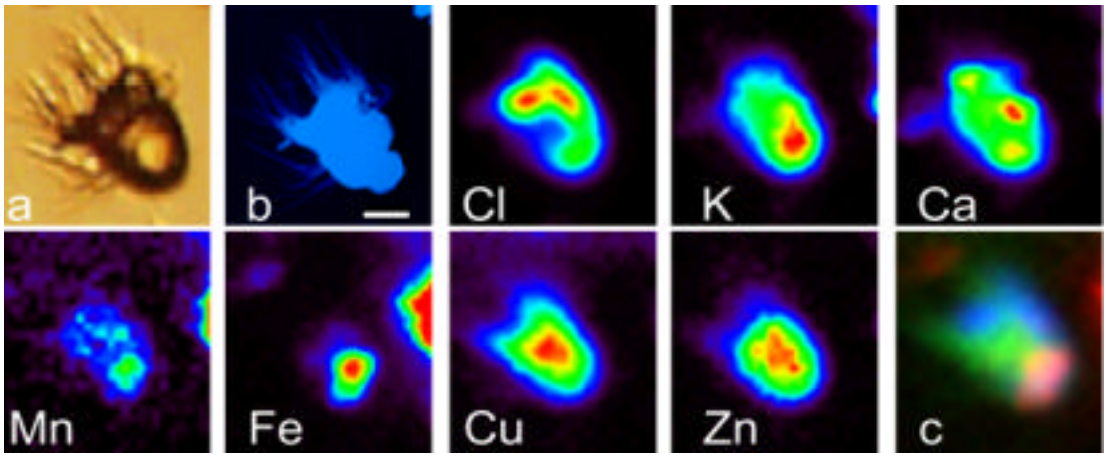

Fig. 1.16. Elemental maps of a marine ciliate (scale bar is 6 μm) collected off Southampton, NY. (a) Light micrograph. (b) Carbon content of the cell as measured by a scanning transmission x-ray microscope. Succeeding images (Cl, K, Ca, Mn, Fe, Cu, Zn) show elemental fluorescence uncorrected for background or spectral overlap. (c) Superposition of the Cl (blue), Fe (red), and Cu (green) images. Cl was chosen as a proxy for cellular biomass, while Fe and Cu trace metals show notably different spatial distributions within this cell.

In order to better understand the interactions between aquatic protists and both nutrient and contaminant trace metals, we have been measuring the elemental compositions of natural bacteria, algae, and their protozoan predators. Preliminary work using radioisotopes suggests that many metals do not absorb effectively onto bacteria and that protozoan predators are much more effective at concentrating certain trace metals from food than are metazoans. Microfluorescence studies (Fig. 1.16) allow us to determine if natural bacteria, photosynthetic algae, and nonphotosynthetic protozoa differ substantially in their trace-element concentrations and to predict more accurately the fate of trace metals incorporated into planktonic ecosystems. Cell-specific element analyses of phytoplankton will also allow us to determine the degree to which variability in algae species composition can affect the transfer of metals from the dissolved phase to higher organisms (e.g., fish). These data will greatly advance our knowledge of the factors that control the cycling of trace elements through food webs.

1.6.3 Quantitative 3D Submicron Phase Tomography

The significant increase in coherence obtained using third-generation synchrotrons, such as the APS, has driven major advances in phase imaging, which offers reduced radiation damage and the ability to observe object features with negligible absorption contrast. In recent years, research in this field has focused on development of accurate and rapid numerical methods (Paganin & Nugent, 1998) to extract the full complex refractive index of the object under study.

Previously, we demonstrated quantitative nanometer-scale two-dimensional (2D) x-ray phase microscopy at beamline 2-ID-B. We recently used the same optical system to perform tomographic phase imaging in three dimensions. In this experiment, a coherent 1.83 keV x-ray beam illuminated a sample consisting of a 9-μm-long commercial atomic force microscope (AFM) tip. A zone-plate lens magnified the object by 160 times onto an x-ray CCD camera, providing an image resolution of ~150 nm. To obtain the phase information, two defocused images were recorded on either side of the in-focus position by translating the zone plate along the optical axis. Two-dimensional projected phase maps were obtained from the defocus data after cropping and equilibration to compensate for beam intensity variations. This process was repeated at 1° intervals over a 180° angular range about the sample, then the phase data were aligned and reconstructed into three-dimensional (3D) images using the filtered back-projection method (Fig. 1.17). The resolution in these images is better than 900 nm, evidenced by the 6 pixel diameter of the spherical bump (a manufacturing defect) visible in Figs. 1.17b-f. The apparent faceted nature is typical of the manufacturing process used to etch crystalline AFM tips.

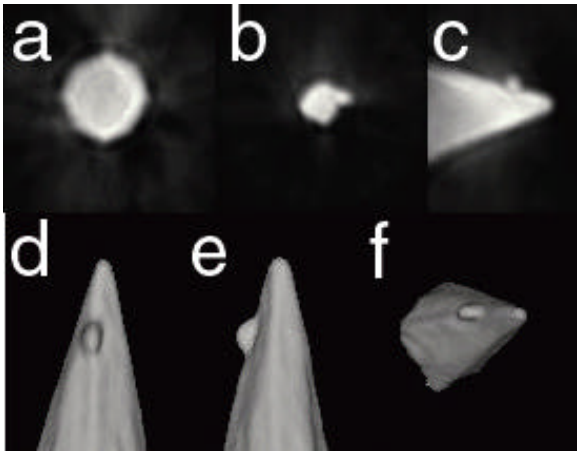

Fig. 1.17. Quantitative 3D reconstructions of the real part of the refractive index of the AFM tip. (a) Horizontal slice of the AFM tip. (b) A second slice including the spherical bump. (c) Vertical slice through the tomographic phase data. (d-f) Volume renderings of the AFM tip.

The reconstructed phase data yielded a measured refractive index decrement of $\delta=(5.0\pm0.5)\times10^{-5}$. The calculated value of $\delta=5.06\times10^{-5}$ at 1.83 keV, based upon the known composition of the AFM tip, is well within experimental error (McMahon et al., submitted).

1.6.4 Fast Tomography

Anatomical research in millimeter-scale organisms is notoriously time consuming. Because they may be too small to prepare directly and too large for, e.g., confocal microscopy, anatomical examination of such samples is traditionally done by preparation and analysis of histological sections, which are then reconstructed in 3D. Mechanical artifacts arising from the cutting process hinder fidelity and automation of the reconstruction, and a histological section series typically takes a week or more to acquire. In comparison, hundreds of specimens can be imaged in a typical run of 48-72 h using the fast microtomography system at beamline 2-BM. Using the ostracod *Scutigera coleoptrat* as a model sample, M. Fanenbruck (Ruhr U.) compared x-ray microtomography to conventional micro-anatomical methods. Unprocessed tomographic projections taken with 7.5 keV x-rays showed an impressive number of anatomical details, which would be invisible by light microscope. For example, some muscle bundles showed myostriation (Z-band distance of ~2.5 µm), confirming the spatial resolution was ~1 µm. By comparing the tomographic data (Fig. 1.18, left) to histological sections, we observed that almost all tissues were clearly discernible. Phase-contrast tomography or tissue-specific staining (e.g., with heavy-metal coupled antibodies) to enhance the contrast of soft tissues are promising future avenues.

Understanding biomineralization is essential to achieving controlled synthesis of complex biomimetic structures. Sea urchin ossicles are an important model because many aspects of echinoderm calcification resemble those in mammilian dental systems. For example, sea urchin teeth contain a wealth of structure evolved to enhance feeding efficiency. S. Stock (Northwestern U.) is using micro-tomography to study the strategies that sea urchins use to optimize biomechanical strength and toughness. In the sea urchin *(Lytechinius variegatus)* tooth fragment in Fig. 1.18 (right), the two rows of dark features are channels extending through the mineral. These features appear not to have been noted previously and may play an important role in nutrient or other transport within the tooth (Stock et al., submitted). Previous tomographic data revealed only faint bands from these rows, preventing correct interpretation of the structure.

Studies of new ceramic coatings developed at NIST, in collaboration with J. Ilavsky (SUNY/Stony Brook), seek to improve the efficiency and longevity of turbine engine components (Ilavsky et al., submitted). Electron-beam physical-vapor-deposited (EBPVD), yttria-stabilized zirconia (YSZ) thermal barrier coating deposits are used in turbine engines to protect intermetallic materials of turbine blades from hot gasses, resulting in an increased efficiency, reliability, and reduction of environmentally unfriendly gasses, such as NO_x. Figure 1.19 shows a fine columnar structure with small inter-columnar pores in the substrate of such a coating, while at top, the columns and voids are much larger. This structure was studied as function of deposition method and parameters, as well as function of simulated in-service conditions (annealing). The speed of the 2-BM system has proven instrumental to obtain a good statistical base by analyzing a large number of samples.

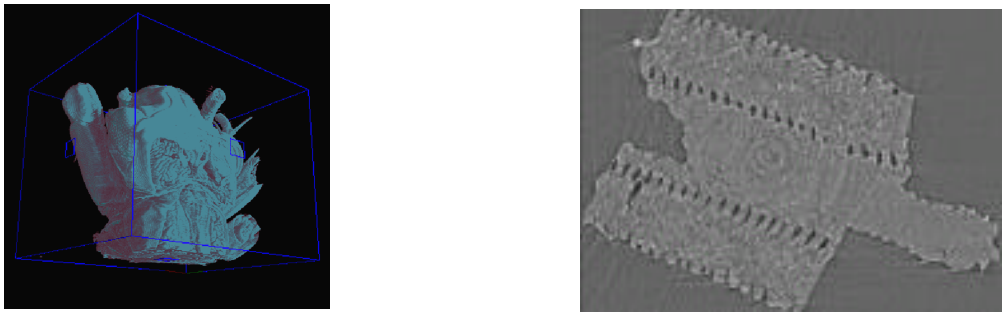

Fig. 1.18. Left: 3D visualization of the ostracod data with gray-scale segmentation of cuticle (cyan) and soft tissues (red). Right: Reconstructed slice of a sea urchin tooth fragment.

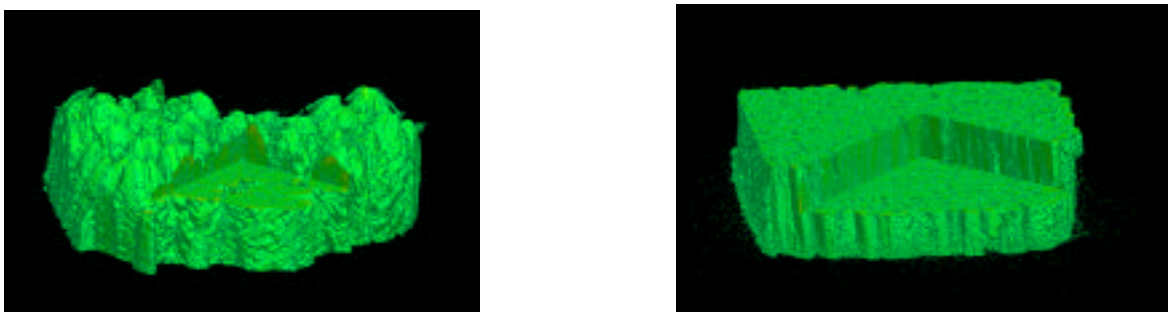

Fig. 1.19. Reconstructed 3D images of EBPVD-YSZ thermal barrier coatings. Left: Image showing structure at the top of the coating. Right: Image showing the structure of the same deposit at the substrate.

1.7 Diffraction and Coherent Scattering

Microdiffraction and coherent scattering methods that take advantage of high-resolution focusing optics and the APS brilliance are important components of the X-ray Microscopy Group user program. Recent highlights include diffraction imaging of antiferromagnetic domains, observation of columnar features in step-graded semiconductor films, combinatorial structure-property mapping of a binary alloy, phase-contrast imaging of defects in macro-molecular crystals, and measurement of x-ray speckle contrast shifts at absorption edges.

1.7.1 Microdiffraction Imaging of Antiferromagnetic Domains

Antiferromagnetic ordering refers either to existing interpenetrating sublattices of identical structure of local magnetic moments with opposite direction or to a zero total spin moment even though the spin density does not vanish. There have been few applications of antiferromagnets because the net magnetic moment is almost always zero at a practically accessible length scale and because they have been extremely difficult to image. We developed a new x-ray microdiffraction technique that makes it dramatically easier to map and analyze antiferromagnetic structure. We used it to reveal the broadening of the first-order "spin-flip" (SF) transition at 123 K in chromium, across which the spins rotate